Unravelling guest dynamics in crystalline molecular organics using solid-state NMR and molecular dynamics simulation.

Valentina Erastova[1,2], Ivana R. Evans[1], William N. Glossop[1], Songül Guryel[1], Paul Hodgkinson[1]*, Hannah E. Kerr[1], Vasily S. Oganesyan[3]*, Lorna K. Softley[1], Helen M. Wickins[1], and Mark R. Wilson[1]

1. Department of Chemistry, Durham University, Stockton Road, Durham, DH1 3LE, UK

2. Department of Chemistry, University of Edinburgh, Joseph Black Building, David Brewster Road, Edinburgh EH9 3FJ, UK

3. School of Chemistry, University of East Anglia, Norwich, NR4 7TJ, UK

ABSTRACT: Solid-state NMR and atomistic molecular dynamics (MD) simulations are used to understand the disorder of guest solvent molecules in two cocrystal solvates of the pharmaceutical furosemide. Traditional approaches to interpreting the NMR data fail to provide a coherent model of molecular behaviour and indeed give misleading kinetic data. In contrast, direct prediction of the NMR properties from MD simulation trajectories allows the NMR data to be correctly interpreted in terms of combined jump-type and libration-type motions. Time-independent component analysis of the MD trajectories provides additional insight, particularly for motions that are invisible to NMR. This allows a coherent picture of the dynamics of molecules restricted in molecular-sized cavities to be determined.

1. INTRODUCTION

Molecular materials often contain disorder, and this disorder may contribute significantly to the relative free energies of different solid forms at ambient temperatures. In the context of pharmaceutical materials, disorder is generally perceived as a risk factor, as it is assumed to reflect metastability with respect to some fully ordered structure. Hence reducing disorder, e.g. via co-crystallisation, is generally perceived as desirable[1].

Disorder is especially common in solvate forms, which are commonly encountered in pharmaceutical chemistry; for example, it has been estimated that up to a third of all active pharmaceutical ingredients (APIs) can form hydrates.[2] Solvates are frequently encountered when the host crystal lattice packing is relatively inefficient, resulting in channels or voids in the structure that can be filled by small molecules, reducing the free energy of the crystal compared to the non-solvated form.[3] Moreover, the solvent is frequently dynamic, potentially providing entropic stabilisation. Hence, disorder may be intrinsic to the stability of the phase and not necessarily a marker of instability. Even if solvate forms are not the final API, they are frequently encountered during pharmaceutical production, and so understanding such forms is important for the characterisation of a drug substance and its production.

Characterising the behaviour of disordered guest solvent is often challenging. Bragg scattering is disrupted by dynamic disorder, and solvent molecules commonly appear in diffraction-derived structures as ill-defined volumes of electron density. NMR provides an alternative, and often more direct route to characterising disordered materials[1,4,5], including identifying and studying the behaviour of solvent molecules in a host crystal structure. Deuterium (^{2}H) NMR is particularly useful, since it is straightforward and inexpensive to introduce ^{2}H isotopic labels using deuterated solvents, and the ^{2}H NMR parameters and spectra are affected by dynamic processes on a broad range of timescales.[6,7] Dynamics on a similar rate to the width of ^{2}H NMR spectra (10–100s kHz) results in changes to the ^{2}H NMR spectrum lineshape, which can potentially distinguish between alternative motional models, while spin-lattice (T_1) relaxation times are sensitive for faster dynamics (on the order of the ^{2}H NMR frequency, typically 100s MHz). The NMR data cannot, however, be directly "inverted" to obtain the molecular motions involved. Relaxation data is particularly difficult to interpret, and even apparently distinctive changes in ^{2}H spectral lineshape can lead to over-simplified models of the molecular behaviour (as discussed below). Hence, it is desirable to use computational chemistry methods to predict molecular behaviour and to link theory and experiment without needing to postulate motional models.
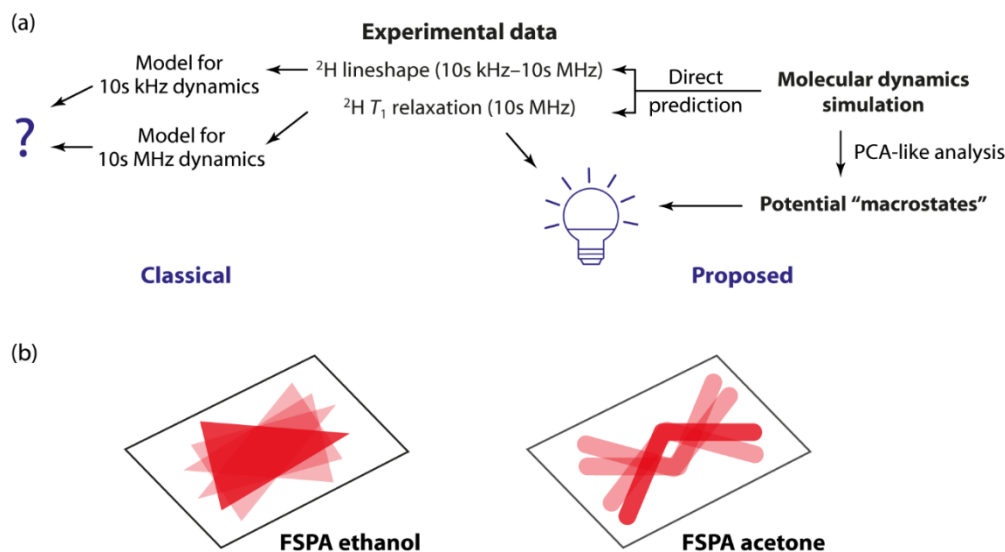
Figure 1. Overview of paper. (a) In classical approaches, ^2H NMR data is analysed using distinct models relevant for 10s kHz and 10s MHz dynamics for lineshape and relaxation data respectively. Particularly when the motion is complex, reconciling these pictures can be difficult or impossible. Here we directly predict of lineshapes and relaxation data from the MD trajectories, avoiding the troublesome "dissection" of the classical approach. (b) Cartoon representation of the resulting physical picture. Since the voids occupied by the solvent molecules have inversion symmetry, and the overall dynamics of the solvent mirrors this symmetry. In both cases, the motion has a strong librational character, but a complementary PCA-like analysis also identifies distinct "macrostates" that reflect the local symmetry of the solvent sites.

In contrast to other domains, such as biomolecular systems, molecular dynamics (MD) simulations have been used relatively sparingly in solid systems. Although there was some scepticism that atomistic force fields would reproduce experimental behaviour in crystalline materials[8], there are now many successful examples of the application of MD to solids containing disorder. For example, MD has been applied to glassy molecular solids, showing that well-chosen force fields can accurately reproduce experimental ^{13}C NMR shift distributions[9,10]. Similarly, averaged NMR parameters derived from MD simulation have been used to understand the dynamics of molecules on catalytic surfaces[11,12], lipid membranes[13,14], and ionic liquids[15]. Most applications to highly crystalline systems have involved porous or channel-containing host-guest systems. For example, the fast rotational and translational dynamics of urea inclusion systems can be effectively studied by conventional atomistic MD, see Ref. [16] and references therein. Studies of gas absorption and diffusion in metal-organic frameworks use different approaches to simulation, notably Grand Canonical Monte Carlo simulations[17,18]. A variety of methods have been used to study the dynamics of so-called "amphidynamic" crystals[19–21], solid systems which contain highly mobile components alongside a rigid molecular framework. Typically, the experimental rate information is derived from NMR, either ^1H T_1 relaxation rates or ^2H NMR spectra[22]. Such materials have been proposed as "molecular machines", e.g. crystalline molecular gyroscopes[22], in which a molecular fragment (a "rotor") is relatively free to rotate, or molecular gears[23–25], in which there is interaction between mobile components. Especially in the latter case, simulations of larger box sizes are needed to understand to the effects of correlation between different rotors[24–26]. Correlated motions often require techniques such as metadynamics[24,27] to enhance sampling beyond standard MD, and to improve the sampling of dynamical pathways on complex free energy surfaces.

In the case of "molecular machines", the motion of the fragment is well defined, and the challenge is to determine the rate of motion and how this is influenced by molecular interactions. In the case of pharmaceutical solvates, the nature of the guest molecule motion is undefined, and it is not obvious how to use molecular dynamics trajectories to derive a physical picture of the motion or compare to experiment. DMSO molecules have been observed to rotate through 180° in MD simulations of a DMSO solvate of carbamazepine, allowing the experimental crystallographic data to be rationalised[28]. MD simulations have been used in a similar way to rationalise experimental data on the dynamics of pyridinium cations obtained from quasi-elastic neutron scattering[29–31], and ^{19}F NMR relaxation data observing molecular motion in solid octafluoronaphalene[32].

And so, while MD has been regularly applied to solid crystalline materials, and NMR is widely used to obtain information (such as activation barriers) from materials exhibiting dynamics, the general question of how to determine the nature of motion of guest molecules moving in a host cavity has not, to our knowledge, been directly addressed. As illustrated schematically in Figure 1, a typical approach is to fit the NMR data, whether spectral line-

2

shapes or relaxation times, to simple motional models. These models are either assumed or obtained qualitatively from simulation methods. Here we present a new approach to predicting ²H NMR lineshapes directly from the results of MD simulations, and show that the direct prediction of ²H spectral and lineshape data provides a more complete physical picture than indirect comparisons involve simplified models.

This methodology is illustrated using a previously unreported co-crystal (FSPA) formed between furosemide (FS) and picolinamide (PA). ²H solid-state NMR and molecular dynamics simulations are used to probe the behavior of FSPA with acetone and ethanol as the solvent guest. The direct prediction of the NMR data from MD simulation, combined with a complementary principal component-type analysis, allows the overall molecular behavior to be understood in terms of the local site symmetry. This methodology can be readily applied to other solid systems in which guest molecules are moving within cavities.

2. METHODS

2.1 Synthesis and crystallography Furosemide is an important pharmaceutical, listed in the World Health Organization's List of Essential Medicines, primarily used in relieving fluid accumulation (edema) in the heart, liver or kidney. Cocrystallisation of furosemide has been widely investigated as a route to improving its relatively poor aqueous solubility.[33–35] Under its synthesis conditions, described in section 1 of the Supplementary Information, the furosemide picolinamide co-crystal readily forms a solvate phase.

Single-crystal diffraction (SCXRD) studies of these materials, discussed in Section 2 of the Supplementary Information, reveal that the FSPA acetone and ethanol solvates are isostructural. Fourier difference maps revealed electron density that is separate from the FS and PA framework, which is assumed to correspond to the solvent, but the geometry could not be refined for either solvent molecule. Having confirmed the presence of solvent using solid-state NMR (cf. Fig. S2), the SCXRD structures were solved with the PLATON SQUEEZE approach.[36] As illustrated in Figure 2, the unit cell contains two pairs of symmetry-equivalent FS and PA molecules and a void at an inversion centre in which the additional electron density resides, suggestive of a channel solvate. The sulfonamide group is refined with disorder over two positions with (fixed) equal occupancies.

2.2 Solid-state NMR High-resolution solid-state NMR spectra were obtained using either a Bruker Avance III HD spectrometer operating at ¹H, ¹³C and ²H NMR frequencies of 499.70 MHz, 125.65 MHz and 76.71 MHz respectively, or a Bruker Avance III HD spectrometer operating at the corresponding frequencies of 400.17 MHz, 100.62 MHz and 61.42 MHz. Samples were packed into 4 mm zirconia rotors. The ¹³C shift scale was referenced with respect to neat tetramethylsilane (TMS) by setting the highest frequency peak of adamantane to 38.5 ppm. The ¹³C spectra were used to fingerprint the structure and assess stability with respect to solvent loss; see Section 3 of the Supplementary
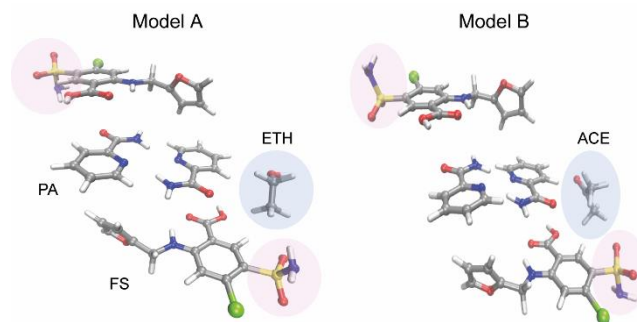
Figure 2 Illustrations of the structure of the ethanol (ETH) and acetone (ACE) furosemide (FS) picolinamide (PA) cocrystal solvates derived from single-crystal XRD experiments at 120 K. Disorder of the sulfonamide group was modelled with a 50:50 split site model, which was resolved into two models, A and B, depending on whether the NH_2 of the sulfonamide points towards the solvent channel (A) or away from it (B). The volume occupied by solvent (highlighted in blue) could not be modelled in the diffraction study. See Figure S1 in the Supplementary Information for an alternative crystallography-oriented depiction of the structure.

Information for further details. The ²H shift scale was referenced with respect to neat TMS by setting the peak of D_2O to 4.81 ppm. Temperatures are quoted to the nearest 5 K to reflect uncertainties in absolute temperature calibration (details of the temperature calibration can be found in the data archive).

Variable-temperature ²H wideline (static) spectra and T_1 relaxation data were acquired at 76.71 MHz for the FSPA-acetone-d_6 sample and 61.42 MHz for the FSPA-ethanol-d_2 sample. FSPA-ethanol-d_2 spectra used 0.2–0.5 s recycle delay and a 40 µs echo delay. FSPA-acetone-d_6 spectra used a 1 s recycle delay and 60 µs echo delay. T_1 relaxation measurements were performed using a saturation recovery sequence for both samples, and single exponential decays were fitted to the integral of the complete bandshape / sideband pattern as a function of recovery time. Excellent single-exponential fits were obtained at all temperatures on both samples. FSPA acetone-d_6 was measured under static conditions using 16 increments and a sample maximum recovery time ranging from 1.8–3.2 s. FSPA ethanol-d_2 was measured under 10 kHz MAS using 16 increments and a sample maximum recovery time ranging from 0.26–0.85 s. The temperature dependence of the relaxation times was fitted assuming a simple Arrhenius-like dependence of the motional correlation time, τ_c, on temperature. The temperature dependence of τ_c was parameterised using the parameters, T_{min} and E_a:

$$\tau_c = \frac{1}{2\pi\nu_0}\exp\left(\frac{E_a}{R}\left(\frac{1}{T} - \frac{1}{T_{min}}\right)\right) \qquad (1)$$

where ν_0 is the ²H NMR frequency. As discussed in Section 4 of the Supplementary Information, this parameterisation reduces the correlation between fitted variables and allows uncertainties to be propagated without the need for Monte Carlo simulations. ¹³C T_1 relaxation times were measured on FSPA ethanol under MAS conditions, but the

3

data was significantly lower quality and is not considered further.

2.3 Molecular dynamics simulations Simulation models for the two FSPA solvates were built using the atomic coordinates and unit cell parameters obtained by XRD at 120 K (corresponding CIF files are supplied in the data archive). An ethanol or acetone solvent molecule was manually placed in the void in the FSPA unit cell (i.e., modelling 100% solvent occupancy), and simulation boxes were made up of 9 x 3 x 3 unit cells and contained 162 FS, 162 PA and 81 solvent molecules. To assess the importance of the sulfonamide disorder depicted in Fig. 2, pairs of simulations were created for both systems, containing uniquely one orientation or the other, with the NH_2 of the sulfonamide either facing pointing towards the solvent channel (model A) or away from it (model B). Although the physical system will contain a random distribution of sulfonamide orientations, these artificial fully ordered systems can be expected to span the range of possible solvent dynamics.

MD simulations were performed with the GROMACS 2016.4 suite,[37,38] using the GAFF force field[39] obtained from the AmberTools 18 package with the AM1-BCC charge model.[40] Each simulation was first energy minimized using the steepest descents algorithm. FS and PA molecules were then positionally restrained using the LINCS algorithm, while the solvent molecules were allowed to move freely and relax into equilibrium positions. The system was pre-equilibrated for 1 ns in the *NPT* ensemble with the velocity-rescale Berendsen thermostat at 120 K, with a temperature coupling constant of 0.1 ps, and an isotropic Berendsen barostat applied with a reference pressure of 1 bar and a pressure coupling constant of 20 ps. The positional restraints on the FS PA were then removed after the solvent molecule relaxation, and the whole system allowed to equilibrate for an additional 1 ns with the same protocol as above, with the temperature set to 120 K, as in the original crystal structure determination.

This initial equilibration was followed by an annealing run heating the system from 120 K to 350 K, in steps of 30 or 50 K over 10 ns, followed by 10 ns relaxation to prevent a hysteresis before the next temperature increment. H-heteroatom bonds were constrained using the LINCS algorithm, other parameters as above. Structures were extracted at the temperatures of 150 K, 200 K, 250 K, 300 K and 350 K, and then simulated in the *NPT* ensemble with the Nosé-Hoover thermostat at the given temperature with a temperature coupling constant of 1 ps, and an anisotropic Parrinello-Rahman barostat employed at 1 bar, with a pressure coupling constant of 20 ps. Production simulations runs were performed for 200 ns without bond constraints. The 150 K simulation was extended to 400 ns for improved sampling statistics.

The experimental and predicted densities at 120 K are in reasonably good agreement (3–5% deviation from Table S3). The deviations could result from several factors, including experimental uncertainties in the exact temperature of the crystal in the SCXRD measurements, the non-stoichiometry of the solvent loading, and the use of the GAFF force field at low temperature (noting that GAFF is parametrised at higher temperatures where atoms sit at slightly different average positions in their potential wells). We argue below that the reproduction of the experimental NMR data provides a more direct measure of the effectiveness of the force field performance.

The resulting trajectories were analysed using two approaches: direct prediction of the NMR results from the trajectories (described below) and a Markov State Modelling (MSM). These MSM analyses were performed using the PyEMMA 3.5.4 package.[41] Two vectors describing each solvent molecule were extracted from the MD trajectories and used for featurization. This approach offers a dimensionality reduction by removing unnecessary atomic coordinates and significantly speeds up data processing[42]. The time-lagged independent component analysis method (TICA) was used to decouple any fast vibration-like motions from the significant solvent reorientations.[43] The resulting TICs were then used to derive Markov state models, using k-means clustering to discretise the data to a representative set of microstates. An appropriate MSM lag time was determined to be 5 fs (10 timesteps) for both the acetone and ethanol systems based on implied timescales plots. Perron-cluster-cluster analysis (PCCA+) was used to cluster the microstates into a limited number of macrostates.[44] Chapman-Kolmogrov (CK) tests[45] were used to validate the resulting Markov state models, and Transition-path theory (TPT) was applied to determine the flux between macrostates[46–48] ; see Section 7 of the Supplementary Information for further details.

2.4 Prediction of NMR spectra from MD simulations Simulation methodology developed previously for predicting EPR spectra of molecular systems with introduced spin labels and probes from MD trajectories[49,50] has been adapted for the simulation of ^{2}H NMR lineshapes. The MD-EPR methodology has been successfully applied to various complex molecular systems, including proteins, liquid crystals, lyotropic mesophases, lipid membranes and DNA fragments.[51–55] This trajectory-based approach employs the Liouville von Neumann equation in the semi-classical approximation, often called the Langevin form of the Stochastic Liouville Equation:[50]

$$\frac{d\boldsymbol{\rho}(t)}{dt} = -i\hat{\hat{L}}(t)\boldsymbol{\rho}(t) \qquad (2)$$

where $\boldsymbol{\rho}$ is a density matrix of the system and the Liouvillian $\hat{\hat{L}}$ is a superoperator of the interaction Hamiltonian, expressed in the units of $\hbar$.

^{2}H NMR probes dynamics via the coupling between electric field gradient tensor, **V**, at the given site and the nuclear electric quadrupolar moment. Ignoring the effects of longitudinal relaxation, the only non-zero matrix elements of $\hat{\hat{L}}$ relevant for the time evolution of the transverse magnetisation involve:

$$\nu_{\pm 1}(t) = \pm \tfrac{3}{8}\chi\big((3\cos^2\beta_{\mathrm{P}\to\mathrm{L}}(t) - 1) - \eta\sin^2\beta_{\mathrm{P}\to\mathrm{L}}(t)\cos 2\gamma_{\mathrm{P}\to\mathrm{L}}(t)\big) (3)$$

which are the frequencies of the two allowed NMR transitions for $I = 1$, and χ and η are the conventional parameters defining the magnitude of the EFG tensor **V** (see Sec-

4

tion 5 of the Supplementary Information). For each time point along the MD trajectory, the Euler angles $\Omega_{P\to L}(t)$ define the passive rotation from the interaction PAS frame to the laboratory-fixed frame.

As shown by Oganesyan[49,50], the evolution of the spin density matrix in the fast motional limit can be calculated using the expression:

$$\boldsymbol{\rho}(t) = \exp\left(-\left[i\langle\hat{\hat{L}}\rangle + \hat{\hat{\Lambda}}\right]t\right)\boldsymbol{\rho}(0) \qquad (4)$$

The first term in the matrix exponential, $\langle\hat{\hat{L}}\rangle = \frac{1}{\tilde{T}}\int_0^{\tilde{T}}\langle\hat{\hat{L}}(\tau)\rangle\,d\tau$, is a Liouvillian which is averaged over the time of complete relaxation of the correlation function of the molecular motion ($\tilde{T} \approx 10\tau_c$) and over the N copies of the molecules in the simulation; this describes the "average" evolution. This first term is equivalent to deriving averaged NMR parameters from molecular trajectories[11], which is sufficient is if the correlation times are extremely short. In the context of ^{2}H NMR, however, it is important to describe the line-broadening effects of the dynamics, which is captured by the "decoherence matrix" $\hat{\hat{\Lambda}} = \int_0^{\tilde{T}}\langle\Delta\hat{\hat{L}}(0)\Delta\hat{\hat{L}}(\tau)\rangle\,d\tau$ of the second term. $\Delta\hat{\hat{L}}(\tau) = \hat{\hat{L}}(\tau) - \langle\hat{\hat{L}}\rangle$ defines the dephasing of the magnetisation caused by the modulation of $\hat{\hat{L}}(\tau)$ due to the re-orientational dynamics of the molecule.

There are two advantages of using Eq. (4) over direct integration of Eq. (2). Firstly, it offers significant reduction in the overall simulation time compared to full propagation of the density matrix along the entire sampling time. Secondly, long sampling times of up to milliseconds are required to accurately simulate ^{2}H NMR lineshapes, which is impractical for many MD simulations. The use of Eq. (4) allows predictions of NMR data from relatively short MD trajectories (up to the point when autocorrelation functions of rotational dynamics are fully relaxed)[50]. As discussed in Section 5 of the Supplementary Information, this approach is also distinct from simulations of intermediate timescale dynamics in ^{2}H NMR using Markov models.

The following procedure is used to calculate the NMR response for a given MD trajectory. Trajectories from all individual molecules are first concatenated into a single continuous one by performing appropriate rotational transformations. Then the quadrupolar coupling tensor is averaged according to the following equation[53]:

$$(\mathbf{V}^A)_{ij} = V_{XX}^P\langle l_{xi}l_{xj}\rangle + V_{YY}^P\langle l_{yi}l_{yj}\rangle + V_{ZZ}^P\langle l_{zi}l_{zj}\rangle \qquad (5)$$

i.e., time averages are performed on the products of the projection cosines, l_{ij}, of the three PAS axes in the lab frame. The matrix elements of the averaged Liouvillian and the relaxation matrix can then be calculated using the principal values of the motionally averaged tensor, $\mathbf{V}^A$. In particular, the averages of the time-dependent frequencies of Eq. (3) can be written:

$$\bar{v}_{\pm 1}(\Omega_{A\to L}) = \pm\frac{3}{8}\langle\chi\rangle\big((3\cos^2\beta_{A\to L} - 1) - $$
$$\langle\eta\rangle\sin^2\beta_{A\to L}\cos 2\gamma_{A\to L}\big) \qquad (6)$$

where $\langle\chi\rangle$ and $\langle\eta\rangle$ are calculated from the principal values of $\mathbf{V}^A$ (cf. Eq. S1), and $\beta_{A\to L}$ and $\gamma_{A\to L}$ are Euler angles de-

fining the orientation of the laboratory z axis in the frame of the principal axes of $\mathbf{V}^A$; this corresponds to the orientation of the crystallite with respect to the lab frame.

The non-zero elements of the decoherence matrix are calculated from:

$$\lambda_{\pm}(\Omega_{A\to L}) = \int_0^{\tilde{T}}\langle\Delta v_{\pm 1}(0)\Delta v_{\pm 1}(\tau)\rangle\,d\tau \qquad (7)$$

where $\Delta v_{\pm 1}(t) = v_{\pm 1}(\Omega_{P\to A}(t); \Omega_{A\to L}) - \bar{v}_{\pm 1}(\Omega_{A\to L})$ and the time averaging in Eq. (7) is performed over rotations in the A frame which are defined by $\Omega_{P\to A}(t)$. The total rotational transformation from the PAS to the lab frame is defined as: $R(\Omega_{P\to L}(t)) = R(\Omega_{A\to L})R(\Omega_{P\to A}(t))$.

The density matrix is propagated according to Eq. (4) using standard numerical approaches, and projected onto the detection operator I_+ to generate the NMR signal, $s(t)$, prior to Fourier transformation into the frequency domain. In this simple case, however, the $\langle\hat{\hat{L}}\rangle$ and $\hat{\hat{\Lambda}}$ matrices are diagonal, with the $\bar{v}_{\pm 1}(\Omega_{A\to L})$ corresponding to the NMR frequencies with associated damping coefficients $\lambda_{\pm}(\Omega_{A\to L})$. Finally, the response is averaged over $\beta_{A\to L}$ and $\gamma_{A\to L}$ angles assuming an isotropic distribution of crystallites in the sample.

This new approach to simulating ^{2}H NMR spectra from MD trajectories method allows lineshapes to be accurately and efficient calculated from MD trajectories of achievable lengths[50].

The χ quadrupolar parameter for FSPA ethanol was taken from a fit of the low temperature experimental data, as shown in Figure S3. The corresponding values for the methyl group of the acetone solvate were taken from the literature[56], with the effect of rapid rotational diffusion accounted for by applying Eq. S2, with the angles $\alpha = 0$, $\beta = 70.50°$, resulting in the values $\chi = 53.25$ kHz, $\eta = 0$.

2.5 Prediction of T_1 relaxation times from MD simulations The longitudinal relaxation times T_1 of ^{2}H due to quadrupolar interactions under the Redfield approximation and in the case of restricted local molecular motions are given by the standard expression[57,58]:

$$\frac{1}{T_1} = \frac{3\pi^2}{20}\chi^2(1 - S^2)\left(1 + \frac{\eta^2}{3}\right)(J(\omega_0) + 4J(2\omega_0)) \qquad (8)$$

where S^2 is the square of the generalised order parameter of the molecular orientations, and $J(\omega)$ is the spectral density function, which is the one-sided Fourier transform of the reorientational correlation function:

$$J(\omega) = 2\int_0^\infty C_2(t)\cos(\omega t)\,dt \qquad (9)$$

and ω_0 is the NMR frequency (expressed as an angular frequency), and the correlation function $C_2(t)$ is defined as:

$$C_2(t) = \lim_{T\to\infty}\frac{1}{T}\int_0^T\langle P_2(\vec{\mu}(\tau)\cdot\vec{\mu}(t+\tau))\rangle\,d\tau \qquad (10)$$

where $P_2(t)$ is a second-order Legendre polynomial and the average is taken over MD simulation time (using a 'sliding time window' approach[50]) and the number of molecules in the system. $\vec{\mu}(t)$ is the unit vector along one of either the equivalent C–D or C–CD$_3$ axes in ethanol and

5

acetone molecules respectively. The one-sided Fourier transformation of the correlation function $C_2(t)$, which combines multiple contributions to the rotational motion of $\vec{\mu}(t)$, is carried out numerically.

To interpret the calculated T_1 values, it is also useful to calculate an effective correlation time of the re-orientational motion from $C_2(t)$ using the expression:

$$\tau_{c,eff} = \frac{\int_0^\infty C_2(t) - C_2(\infty) \; dt}{1 - C_2(\infty)} \tag{11}$$

A corresponding generalised order parameter can be estimated from the correlation function as $S^2 = C_2(\infty)$.

In all cases, MD trajectories of 200 ns in length were sufficient to calculate NMR lineshapes and T_1 relaxation times, except simulations at $T = 150$ K, where extended trajectories of 400 ns were required to adequately capture the much slower re-orientational dynamics of the solvent molecules.

3. RESULTS AND DISCUSSION
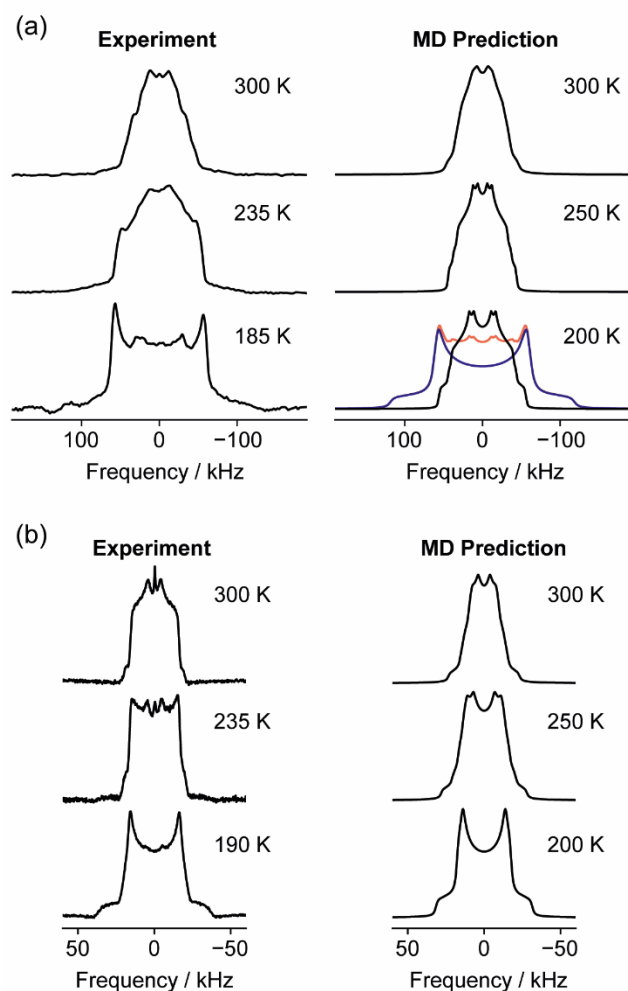
Figure 3 ^{2}H quadrupolar echo spectra of (a) FSPA ethanol-d$_2$ spectra and (b) FSPA acetone-d$_6$. The sharp peak in the centre of the spectra in (b) at 235 K and 300 K probably reflect trace adventitious acetone. The right-hand sides show MD-predicted spectra at the closest matching temperatures. These are 50:50 sums over models A and B; individual contributions from models A and B are shown in Figures S8 and S9 of the SI. The experimental spectrum of the ethanol solvate at 185 K contains a significant contribution from the "frozen limit" lineshape. The total predicted lineshape at 200 K (salmon) is the sum of 20% dynamic component and 80% static compo-
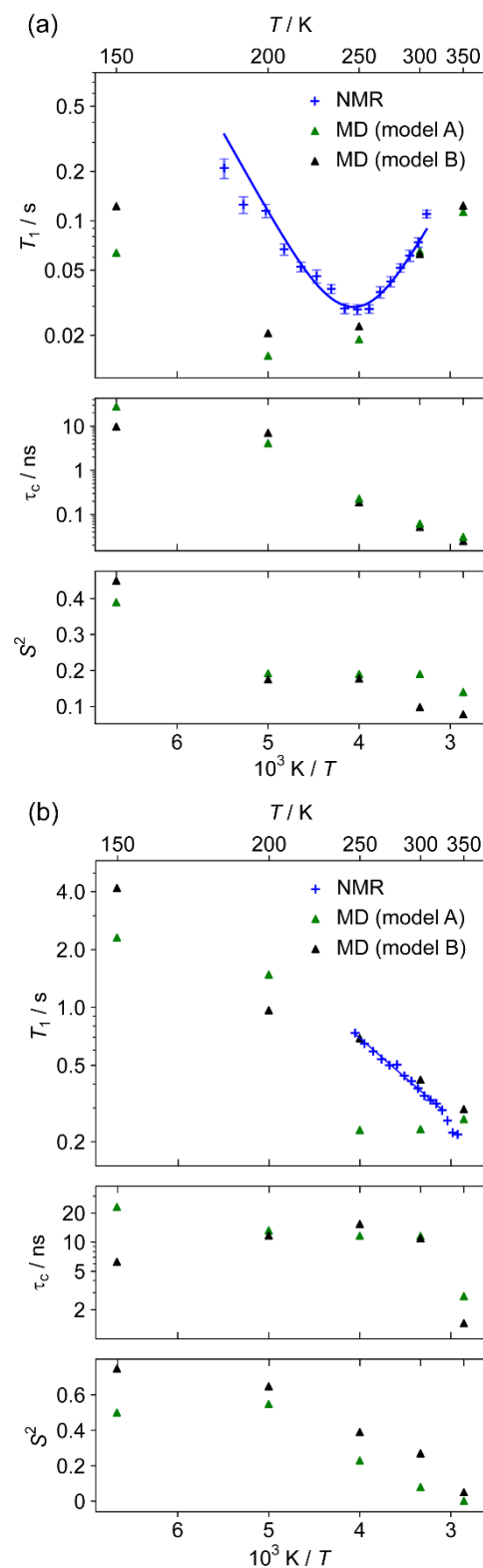
Figure 4 ^{2}H spin-lattice relaxation time constants, T_1, as a function of temperature of (a) FSPA ethanol-d$_2$ acquired at 61.42 MHz and (b) FSPA acetone-d$_6$ at 76.7 MHz. Triangles are predictions from MD simulation. Lower panels show the $\tau_{c,eff}$ and S2 parameters for the motion derived from MD. The curve in (a) is a fit of the experimental data to E_a of 19.0 ± 0.9 kJ mol^{-1} and a T_{min} = 234.0 ± 1.2 K. The experimental data in (b) looks to fit to Arrhenius behavior, but the $\tau_{c,eff}$ values obtained from MD show that the temperature dependence cannot be interpreted in terms of an E_a (see text for further discussion).

The experimental data presented in Figures 3 and 4 appears sufficiently distinctive to be interpreted; there are significant changes in both ^{2}H lineshapes (Figure 3) and in T_1 (Figure 4) with temperature. Indeed, the spectrum of the acetone solvate, Figure 3(b), can be modelled in simple terms; the spectra are relatively narrow at all temperatures, consistent with fast dynamics of the CD_3 groups, and the changes of the spectrum with temperature can be reproduced by a simple two-state Markov model corresponding to "intermediate timescale" C_2 jumps about the C=O axis (see Figure S6 of the Supplementary Information). As shown by the molecular dynamics results, however, this naïve model is incorrect and the jump rates obtained from this widely used analysis are essentially meaningless.

There are also difficulties in interpreting the T_1 relaxation data, Figure 4. Although the temperature dependences can be fitted to Arrhenius behavior, it is not obvious that the parameters obtained relate to molecular behaviour. For example, the activation energy for the acetone motion of 7.9 ± 0.2 kJ mol^{-1} derived from Arrhenius-type analysis is small, and would be expected to correspond to a fast motion, while the sign of the slope implies that the motion is still slow compared the ^{2}H Larmor frequency (10s MHz). This inability to reconcile models of the lineshape and relaxation data taken in isolation was illustrated schematically in Figure 1(a).

In contrast, the comparison between experimental ^{2}H NMR spectra and those predicted from MD trajectories in Figure 3 is highly revealing. The overall qualitative agreement is excellent, showing both that the MD simulations have captured the solvent behavior, and that the calculation methodology introduced in Section 2.2 is appropriate. Note that, as discussed in Section 6 of the Supplementary Information, the rotation of sulfonamide groups is slow in comparison to solvent reorientation. Hence, we provide results that are an average of model A and B simulations, noting that the solvent dynamics are sufficiently similar in these idealised models for the overall trends to be validated. The comparison shows that the experimental spectrum of the ethanol solvate at 185 K contains a significant contribution from the "frozen limit" lineshape corresponding to static ethanol molecules. This behaviour was reproducible, and similar unexpected contributions from "frozen" guest molecules have been observed in other studies, and tentatively rationalised in terms of temperature gradients across the sample[59]. At a very straightforward level, the MD allows this experimental feature to be factored out.

Figures 3 and 4 show that the trends in the experimental data can be reproduced from the MD simulation, but this does not, in itself, provide insight into the nature of the motion. This can be most obviously obtained by analysis of the MD trajectories themselves (as discussed below), but it is also useful to parameterise the correlation functions derived from the MD trajectories in terms of simple restricted rotational diffusion, involving an effective correlation time, $\tau_{c,eff}$, and a generalised order parameter S^2. Given the complexity of the potential surfaces, the correlation functions are not expected to be simple exponentials (ex-

amples are shown in Figure S10 of the Supplementary Information), but the general trends in τ_c and S^2, shown in the lower panels of Figure 4 (and tabulated in Table S6 of the Supplementary Information), are expected to be robust. Notably, *both* parameters vary with temperature. This clearly shows that simple jump-type models, which involve a fixed geometry (amplitude) motion, will not correctly describe the dynamics, even if plausible fits to the experimental data can be obtained (cf. Figure S6). Moreover, the assumption that the correlation time is associated, via an Arrhenius-type relationship, to a thermally activated jump process is clearly incorrect for the acetone dynamics; the $\tau_{c,eff}$ values are essentially independent of temperature over the range 200–300 K, rather it is the amplitude of motion (parameterised by S^2) that changes with temperature. This implies that the acetone dynamics has a strong librational character (only the amplitude and not the frequency of motion changes with temperature for barrierless motions).

The fact that the solvent dynamics involves both libration and jump-type motions is confirmed by comparing the predicted T_1 relaxation times with experimental values in Figure 4. Given that there are no adjustable parameters, there is excellent qualitative agreement when considering the pair of systems. Recalling that the trends in the experimental data could not be rationalised, the fact that MD simulations correctly predict trends in both ^{2}H NMR spectra and relaxation data shows that the simulations are correctly capturing the solvent dynamics. Significantly this dynamics is consistently on a fast NMR timescale, with motional correlation times measured in ns, and so the traditional approach of analysing changes in ^{2}H spectra in terms of intermediate timescale dynamics, cf. Figure 1 (a), is destined to give misleading results.

Additional complementary insight into molecular behavior is provided by a Markov state model (MSM) analysis of the MD trajectories. Figure 5 shows the result of applying the pyEMMA analysis suite to the solvent molecule MD trajectories. In the case of the acetone solvate, two components are identified that account in total for > 95% of the variance of the motion. A free energy plot obtained by projecting the trajectories into this space, Figure 5 (a), shows four distinct minimum energy states. As illustrated in Figure S15 of the Supplementary Information, the MD trajectory can be clustered according to these states, allowing representative snapshots, Figure 5 (c), to be extracted, which correspond to four distinct "orientations" of the acetone within the cavity. These macrostates are related by a C_2 axis (respecting the molecular symmetry) and an inversion centre (respecting the symmetry of the cavity).

7
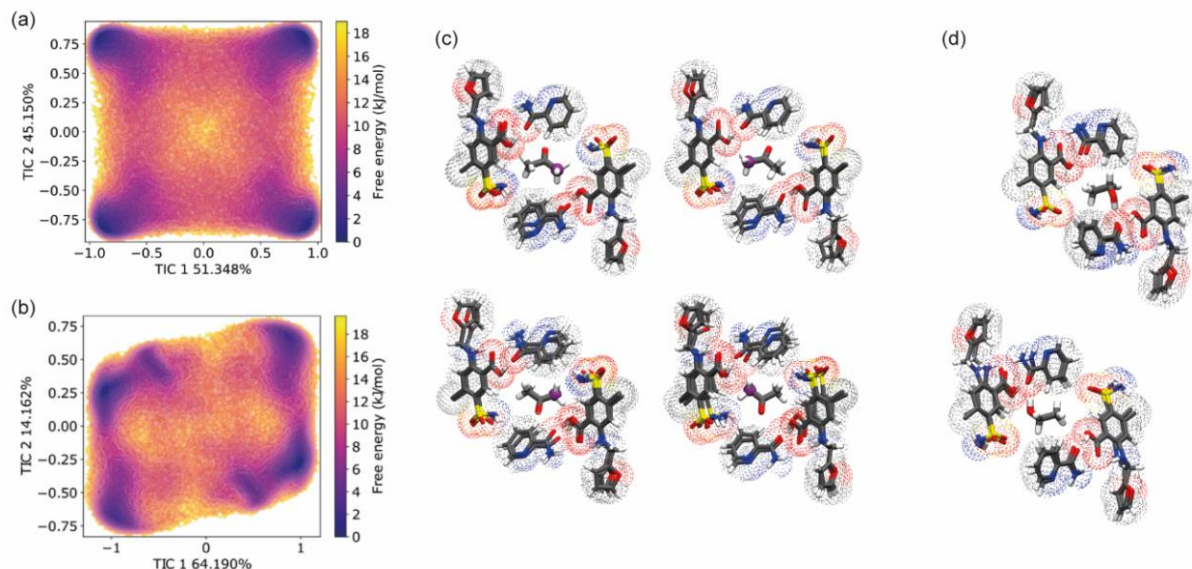
Figure 5 Time Independent Component (TIC) analyses of the FPSA solvate simulations at 273 K. Free energy plots as a function of the first two TICs for (a) FSPA acetone and (b) FSPA ethanol. (c) Representative snapshots of macrostates corresponding to the four free energy minima in acetone. One of the methyl carbons of the acetone is coloured magenta to highlight the reorientation. (d) Representative snapshots of macrostates corresponding to the two free energy minima in ethanol.

The MSM analysis of the ethanol solvates shows that the ethanol motion is complex, with a higher degree of librational character; only 76% of the variance is captured by the first two TICs. There are two distinct macrostates in the free energy plot, Figure 5(b) separated by a 180° rotational flip, as shown in Figure 5(d). Each of these states contains three sub-states corresponding to rotation about the molecular long axis, with H-bonding occurring in each case between the ethanol hydroxyl group and oxygen H-bond donors of FSPA. See Section 7 of the Supplementary Information for more detailed quantitative analysis of the motion.

4. CONCLUSIONS

Two analysis approaches have been applied to molecular dynamics (MD) simulation data to understand the dynamics of solvent molecules in cocrystal solvate materials.

A Markov State Modelling analysis, which has previously been applied mainly to protein dynamics, was successful in identifying stable states, pathways between them and corresponding transition rates. This analysis provided direct insight into slower larger amplitude motions (as distinct from faster motions such as libration), identifying two main states for ethanol within the FSPA structure, and four symmetry-equivalent states for acetone. This two-fold and four-fold degeneracy is consistent with the local molecular and crystallographic symmetry. It is important to note, however, that this insight cannot be obtained from comparing predicted and experimental NMR data, since the ^{2}H quadrupolar tensor is invariant under inversion and so inversion-type dynamics will be invisible to ^{2}H NMR. This weakness is shared with classic approaches to modelling ^{2}H lineshapes using Markov jump-models, where a simplistic model based on C_2 jumps provides a satisfactory (but

ultimately incorrect) fit to the experimental data (cf. Figure S6).

Overall, the solvent disorder is seen to be an intrinsic property of the system that provides some entropic stabilisation, precisely because the symmetry of the solvent and the guest cavity do not match. Similar behavior has been observed in the solvates of droperidol, where the adopted of disordered vs. ordered structures could be rationalised on simple free energy grounds rather than any intrinsic metastability of the disordered structure[60].

Direct simulations of ^{2}H NMR spectral lineshapes and T_1 relaxation times, using methodology previously applied to EPR spectra, clearly show that the MD simulations fully capture the dynamics observed in NMR, and the both the lineshape and relaxation can be explained by the same processes occurring on fast (ns) timescales. Crucially both libration and jump-type motions are treated on an equal footing, avoiding trying to fit lineshapes purely in terms of jump-type models. This explains why traditional approaches to interpreting ^{2}H NMR data gave inconsistent and misleading results, even though good fits could be obtained with individual experimental data sets.

The combination of experiments to provide the overall structure (from single-crystal diffraction) and rate information (^{2}H NMR), together with the analysis of the MD simulations to provide insight into the molecular motion, leads to a powerful methodology to explain the complex motions often seen in solid materials. We anticipate a more complete understanding of dynamics, especially in more complex systems, e.g. involving coupled rotors[26], will be possible by combining sophisticated MD simulation analysis methods and experiment. As well as exploring complex functional materials, robust protocols that confirm the nature and origin of disorder in molecular organics, will be

8

 ORCID: https://orcid.org/0000-0003-0327-3349

important in pharmaceutical applications. Confirming that a disordered material is at a likely thermodynamic minimum provides increased confidence in its overall stability.

ASSOCIATED CONTENT

AUTHOR INFORMATION

Corresponding Authors

* Paul Hodgkinson: paul.hodgkinson@durham.ac.uk
Vasily Oganesyan: V.Oganesyan@uea.ac.uk

Author Contributions

The manuscript was written through contributions of all authors, and all authors have given approval to the final version of the manuscript.

Funding Sources

ACKNOWLEDGMENTS

REFERENCES

(1)   Szell, P. M. J.; Lewandowski, J. R.; Blade, H.; Hughes, L. P.; Nilsson Lill, S. O.; Brown, S. P. Taming the Dynamics in a Pharmaceutical by Cocrystallization: Investigating the Impact of the Coformer by Solid-State NMR. *CrystEngComm* **2021**, *23*, 6859–6870.

(2)   Vippagunta, S. R.; Brittain, H. G.; Grant, D. J. W. Crystalline Solids. *Adv. Drug Deliv. Rev.* **2001**, *48*, 3–26.

(3)   Price, C. P.; Glick, G. D.; Matzger, A. J. Dissecting the Behavior of a Promiscuous Solvate Former. *Angew. Chem. Int. Ed.* **2006**, *45*, 2062–2066.

(4)   Moran, R. F.; Dawson, D. M.; Ashbrook, S. E. Exploiting NMR Spectroscopy for the Study of Disorder in Solids. *Int. Rev. Phys. Chem.* **2017**, *36*, 39–115.

(5)   Apperley, D. C.; Harris, R. K.; Hodgkinson, P. *Solid-State NMR: Basic Principles and Practice*; Momentum Press, 2012.

(6)   Vold, R. L.; Hoatson, G. L. Effects of Jump Dynamics on Solid State Nuclear Magnetic Resonance Line Shapes and Spin Relaxation Times. *J. Magn. Reson.* **2009**, *198*, 57–72.

(7)   Vold, R. R. Deuterium NMR Studies of Dynamics in Solids and Liquid Crystals. In *Nuclear Magnetic Resonance Probes of Molecular Dynamics*; Tycko, R., Ed.; Kluwer Academic Publishers, 1994; pp 27–112.

(8)   Nemkevich, A.; Bürgi, H. B.; Spackman, M. A.; Corry, B. Molecular Dynamics Simulations of Structure and Dynamics of Organic Molecular Crystals. *Phys. Chem. Chem. Phys.* **2010**, *12*, 14916–14929.

(9)   Lefort, R.; Bordat, P.; Cesaro, A.; Descamps, M. Exploring the Conformational Energy Landscape of Glassy Disaccharides by Cross Polarization Magic Angle Spinning ^{13}C Nuclear Magnetic Resonance and Numerical Simulations. II. Enhanced Molecular Flexibility in Amorphous Trehalose. *J. Chem. Phys.* **2007**, *126*, 014511.

(10)   Lefort, R.; Bordat, P.; Cesaro, A.; Descamps, M. Exploring Conformational Energy Landscape of Glassy Disaccharides by Cross Polarization Magic Angle Spinning ^{13}C NMR and Numerical Simulations. I. Methodological Aspects. *J. Chem. Phys.* **2007**, *126*, 014510.

(11)   Paterson, A. L.; Liu, D. J.; Kanbur, U.; Sadow, A. D.; Perras, F. A. Observing the Three-Dimensional Dynamics of Supported Metal Complexes. *Inorg. Chem. Front.* **2021**, *8*, 1416–1431.

(12)   Kobayashi, T.; Liu, D. J.; Perras, F. A. Spatial Arrangement of Dynamic Surface Species from Solid-State NMR and Machine Learning-Accelerated MD Simulations. *Chem. Commun.* **2022**, *58*, 13939–13942.

(13)   Ferreira, T. M.; Topgaard, D.; Ollila, O. H. S. Molecular Conformation and Bilayer Pores in a Nonionic Surfactant Lamellar Phase Studied with ^1H-^{13}C Solid-State NMR and Molecular Dynamics Simulations. *Langmuir* **2014**, *30*, 461–469.

(14)   Fridolf, S.; Hamid, M. K.; Svenningsson, L.; Skepö, M.; Sparr, E.; Topgaard, D. Molecular Dynamics Simulations and Solid-State Nuclear Magnetic Resonance Spectroscopy Measurements of C-H Bond Order Parameters and Effective Correlation Times in a POPC-GM3 Bilayer. *Phys. Chem. Chem. Phys.* **2022**, *24*, 25588–25601.

(15)   Karagianni, M.; Gkoura, L.; Srivastava, A.; Chatzichristos, A.; Tsolakis, N.; Romanos, G.; Orfanidis, S.; Panopoulos, N.; Alhassan, S.; Homouz, D.; Hassan, J.; Fardis, M.; Papavassiliou, G. Dynamic Molecular Ordering in Multiphasic Nanoconfined Ionic Liquids Detected with Time-Resolved Diffusion NMR. *Commun. Mater.* **2023**, *4*, 9.

(16)   Ilott, A. J.; Palucha, S.; Batsanov, A. S.; Harris, K. D. M.; Hodgkinson, P.; Wilson, M. R. Structural Properties of Carboxylic Acid Dimers Confined within the Urea Tunnel Structure: An MD Simulation Study. *J. Phys. Chem. B* **2011**, *115*, 2791–2800.

(17)   Little, M. A.; Cooper, A. I. The Chemistry of Porous Organic Molecular Materials. *Adv. Funct. Mater.* **2020**, *30*, 1909842.

(18)   Witherspoon, V. J.; Xu, J.; Reimer, J. A. Solid-State NMR Investigations of Carbon Dioxide Gas in Metal-Organic Frameworks: Insights into Molecular Motion and Adsorptive Behavior. *Chem. Rev.* **2018**, *118*, 10033–10048.

(19)   Vogelsberg, C. S.; Uribe-Romo, F. J.; Lipton, A. S.; Yang, S.; Hou, K. N.; Brown, S.; Garcia-Garibay, M. A. Ultrafast Rotation in an Amphidynamic Crystalline Metal Organic Framework. *Proc. Natl. Acad. Sci. U S A* **2017**, *114*, 13613–13618.

(20)   Liepuoniute, I.; Jellen, M. J.; Garcia-Garibay, M. A. Correlated Motion and Mechanical Gearing in Amphidynamic Crystalline Molecular Machines. *Chem. Sci.* **2020**, *11*, 12994–13007.

(21)   Catalano, L.; Naumov, P. Exploiting Rotational Motion in Molecular Crystals. *CrystEngComm* **2018**, *20*, 5872–5883.

(22)   Jarowski, P. D.; Houk, K. N.; Garcia-Garibay, M. A. Importance of Correlated Motions on the Low Barrier Rotational Potentials of Crystalline Molecular Gyroscopes. *J. Am. Chem. Soc.* **2007**, *129*, 3110–3117.

(23)   Jellen, M. J.; Liepuoniute, I.; Jin, M.; Jones, C. G.; Yang, S.; Jiang, X.; Nelson, H. M.; Houk, K. N.; Garcia-Garibay, M. A. Enhanced Gearing Fidelity Achieved through Macrocyclization of a Solvated Molecular Spur Gear. *J. Am. Chem. Soc.* **2021**, *143*, 7740–7747.

9

(24) Rodríguez-Fortea, A.; Canadell, E.; Wzietek, P.; Lemouchi, C.; Allain, M.; Zorina, L.; Batail, P. Nanoscale Rotational Dynamics of Four Independent Rotators Confined in Crowded Crystalline Layers. *Nanoscale* **2020**, *12*, 8294–8302.

(25) Lemouchi, C.; Iliopoulos, K.; Zorina, L.; Simonov, S.; Wzietek, P.; Cauchy, T.; Rodríguez-Fortea, A.; Canadell, E.; Kaleta, J.; Michl, J.; Gindre, D.; Chrysos, M.; Batail, P. Crystalline Arrays of Pairs of Molecular Rotors: Correlated Motion, Rotational Barriers, and Space-Inversion Symmetry Breaking Due to Conformational Mutations. *J. Am. Chem. Soc.* **2013**, *135*, 9366–9376.

(26) De Nicola, A.; Correa, A.; Bracco, S.; Perego, J.; Sozzani, P.; Comotti, A.; Milano, G. Collective Dynamics of Molecular Rotors in Periodic Mesoporous Organosilica: A Combined Solid-State ²H-NMR and Molecular Dynamics Simulation Study. *Phys. Chem. Chem. Phys.* **2022**, *24*, 666–673.

(27) Ilott, A. J.; Palucha, S.; Hodgkinson, P.; Wilson, M. R. Well-Tempered Metadynamics as a Tool for Characterizing Multi-Component, Crystalline Molecular Machines. *J. Phys. Chem. B* **2013**, *117*, 12286–12295.

(28) Cruz-Cabeza, A. J.; Day, G. M.; Jones, W. Structure Prediction, Disorder and Dynamics in a DMSO Solvate of Carbamazepine. *Phys. Chem. Chem. Phys.* **2011**, *13*, 12808–12816.

(29) Pajzderska, A.; Gonzalez, M. A.; Wsicki, J. Molecular Dynamics Simulation of Cation Dynamics in Bis-Thiourea Pyridinium Nitrate Inclusion Compound. *J. Chem. Phys.* **2011**, *135*, 074508.

(30) Pajzderska, A.; Gonzalez, M. A.; Wąsicki, J. Dynamics in Molecular and Molecular-Ionic Crystals: A Combined Experimental and Molecular Simulation Study of Reorientational Motions in Benzene, Pyridinium Iodide, and Pyridinium Nitrate. *J. Chem. Phys.* **2013**, *138*, 024508.

(31) Pajzderska, A.; Gonzalez, M. A.; Wsicki, J. In-Plane Pyridinium Cation Reorientation in Bis-Thiourea Chloride, Bromide and Iodide: Quasielastic Neutron Scattering Combined with Molecular Dynamics Simulations. *Phys. Chem. Chem. Phys.* **2012**, *14*, 3949–3959.

(32) Ilott, A. J.; Palucha, S.; Batsanov, A. S.; Wilson, M. R.; Hodgkinson, P. Elucidation of Structure and Dynamics in Solid Octafluoronaphthalene from Combined NMR, Diffraction, and Molecular Dynamics Studies. *J. Am. Chem. Soc.* **2010**, *132*, 5179–5185.

(33) Abraham Miranda, J.; Garnero, C.; Chattah, A. K.; Santiago De Oliveira, Y.; Ayala, A. P.; Longhi, M. R. Furosemide:Triethanolamine Salt as a Strategy to Improve the Biopharmaceutical Properties and Photostability of the Drug. *Cryst. Growth Des.* **2019**, *19*, 2060–2068.

(34) Harriss, B. I.; Vella-Zarb, L.; Wilson, C.; Evans, I. R. Furosemide Cocrystals: Structures, Hydrogen Bonding, and Implications for Properties. *Cryst. Growth Des.* **2014**, *14*, 783–791.

(35) Kerr, H. E.; Softley, L. K.; Suresh, K.; Nangia, A.; Hodgkinson, P.; Evans, I. R. A Furosemide-Isonicotinamide Cocrystal: An Investigation of Properties and Extensive Structural Disorder. *CrystEngComm* **2015**, *17*, 6707–6715.

(36) Spek, A. L. PLATON SQUEEZE: A Tool for the Calculation of the Disordered Solvent Contribution to the Calculated Structure Factors. *Acta Crystallogr. C* **2015**, *71*, 9–18.

(37) Van Der Spoel, D.; Lindahl, E.; Hess, B.; Groenhof, G.; Mark, A. E.; Berendsen, H. J. C. GROMACS: Fast, Flexible, and Free. *J. Comput. Chem.* **2005**, *26*, 1701–1718.

(38) Abraham, M. J.; Murtola, T.; Schulz, R.; Páll, S.; Smith, J. C.; Hess, B.; Lindah, E. Gromacs: High Performance Molecular Simulations through Multi-Level Parallelism from Laptops to Supercomputers. *SoftwareX* **2015**, *1–2*, 19–25.

(39) Wang, J.; Wolf, R. M.; Caldwell, J. W.; Kollman, P. A.; Case, D. A. Development and Testing of a General Amber Force Field. *J. Comput. Chem.* **2004**, *25*, 1157–1174.

(40) Jakalian, A.; Jack, D. B.; Bayly, C. I. Fast, Efficient Generation of High-Quality Atomic Charges. AM1-BCC Model: II. Parameterization and Validation. *J. Comput. Chem.* **2002**, *23*, 1623–1641.

(41) Scherer, M. K.; Trendelkamp-Schroer, B.; Paul, F.; Pérez-Hernández, G.; Hoffmann, M.; Plattner, N.; Wehmeyer, C.; Prinz, J.-H.; Noé, F. PyEMMA 2: A Software Package for Estimation, Validation, and Analysis of Markov Models. *J. Chem. Theory Comput.* **2015**, *11*, 5525–5542.

(42) Goldie, S. J.; Degiacomi, M. T.; Jiang, S.; Clark, S. J.; Erastova, V.; Coleman, K. S. Identification of Graphene Dispersion Agents through Molecular Fingerprints. *ACS Nano* **2022**, *16*, 16109–16117.

(43) Schwantes, C. R.; Pande, V. S. Improvements in Markov State Model Construction Reveal Many Non-Native Interactions in the Folding of NTL9. *J. Chem. Theory Comput.* **2013**, *9*, 2000–2009.

(44) Röblitz, S.; Weber, M. Fuzzy Spectral Clustering by PCCA+: Application to Markov State Models and Data Classification. *Adv. Data Anal. Classif.* **2013**, *7*, 147–179.

(45) Prinz, J. H.; Wu, H.; Sarich, M.; Keller, B.; Senne, M.; Held, M.; Chodera, J. D.; Schtte, C.; Noé, F. Markov Models of Molecular Kinetics: Generation and Validation. *J. Chem. Phys.* **2011**, *134*, 174105.

(46) Metzner, P.; Schütte, C.; Vanden-Eijnden, E. Transition Path Theory for Markov Jump Processes. *Multiscale Model. Simul.* **2009**, *7*, 1192–1219.

(47) Noé, F.; Schütte, C.; Vanden-Eijnden, E.; Renoeich, L.; Weikl, T. R. Constructing the Equilibrium Ensemble of Folding Pathways from Short Off-Equilibrium Simulations. *Proc. Natl. Acad. Sci. U S A* **2009**, *106*, 19011–19016.

(48) Pérez-Hernández, G.; Paul, F.; Giorgino, T.; De Fabritiis, G.; Noé, F. Identification of Slow Molecular Order Parameters for Markov Model Construction. *J. Chem. Phys.* **2013**, *139*, 015102.

(49) Oganesyan, V. S. EPR Spectroscopy and Molecular Dynamics Modelling: A Combined Approach to Study Liquid Crystals. *Liq. Cryst.* **2018**, *45*, 2139–2157.

(50) Oganesyan, V. S. A General Approach for Prediction of Motional EPR Spectra from Molecular Dynamics (MD) Simulations: Application to Spin Labelled Protein. *Phys. Chem. Chem. Phys.* **2011**, *13*, 4724–4737.

(51) Oganesyan, V. S.; Chami, F.; White, G. F.; Thomson, A. J. A Combined EPR and MD Simulation Study of a Nitroxyl Spin Label with Restricted Internal Mobility Sensitive to Protein Dynamics. *J. Magn. Reason.* **2017**, *274*, 24–35.

(52) Prior, C.; Oganesyan, V. S. Prediction of EPR Spectra of Lyotropic Liquid Crystals Using a Combination of Molecular Dynamics Simulations and the Model-Free Approach. *Chem. – Eur. J.* **2017**, *23*, 13192–13204.

(53) Prior, C.; Danilane, L.; Oganesyan, V. S. All-Atom Molecular Dynamics Simulations of Spin Labelled Double and Single-Strand DNA for EPR Studies. *Phys. Chem. Chem. Phys.* **2018**, *20*, 13461–13472.

(54) Catte, A.; White, G. F.; Wilson, M. R.; Oganesyan, V. S. Direct Prediction of EPR Spectra from Lipid Bilayers: Understanding Structure and Dynamics in Biological Membranes. *ChemPhysChem* **2018**, *19*, 2183–2193.

(55) Kuprusevicius, E.; Edge, R.; Gopee, H.; Cammidge, A. N.; McInnes, E. J. L.; Wilson, M. R.; Oganesyan, V. S. Prediction of EPR Spectra of Liquid Crystals with Doped Spin Probes from Fully Atomistic Molecular Dynamics Simulations: Exploring Molecular Order and Dynamics at the Phase Transition. *Chem. – Eur. J.* **2010**, *16*, 11558–11562.

(56) Akbey, Ü. Dynamics of Uniformly Labelled Solid Proteins between 100 and 300 K: A 2D ²H-¹³C MAS NMR Approach. *J. Magn. Reson.* **2021**, *327*, 106974.

(57) Lipari, G.; Szabo, A. Model-Free Approach to the Interpretation of Nuclear Magnetic Resonance Relaxation in Macro-

10

molecules. 2. Analysis of Experimental Results. *J. Am. Chem. Soc.* **1982**, *104*, 4559–4570.

(58) Fung, B. M.; McGaughy, T. W. Study of Spin-Lattice and Spin-Spin in Muscle Water. *Biophys. J.* **1979**, *28*, 293–303.

(59) Shi, C.; Zhang, X.; Yu, C. H.; Yao, Y. F.; Zhang, W. Geometric Isotope Effect of Deuteration in a Hydrogen-Bonded Host-Guest Crystal. *Nat. Commun.* **2018**, *9*, 1–9.

(60) Běrziņš, A.; Hodgkinson, P. Solid-State NMR and Computational Investigation of Solvent Molecule Arrangement and Dynamics in Isostructural Solvates of Droperidol. *Solid State Nucl. Magn. Reason.* **2015**, *65*, 12–20.